Efficacy of an S-Shaped Air Inlet on the Reduction of Front Bistatic Radar Cross Section of a Fighter Engine

Shen Shou Max Chung[1, *] and Shih-Chung Tuan[2]

Abstract—The engine of a fighter plane is one of the largest scattering centers of the entire aircraft. One possible way of reducing the radar cross section (RCS) of the engine is to use an S-shaped bending air inlet to avoid direct radar wave illumination and reflection. We evaluate the efficacy of an S-shaped air inlet on RCS reduction by simulating the boresight and $\pm 15°$ bistatic RCS for a digital model of an engine located behind an S-shaped inlet, using a multi-level fast multipole method (MLFMM) code in the S and X bands. The results show that a curved S-type air inlet can reduce the engine boresight bistatic RCS by ~ 10–$12\,$dBsm at $3\,$GHz, and $\sim 16\,$dBsm at $10\,$GHz when radar wave is incident from boresight, but not to the level required by RF stealth standards. When the radar waves are incident from $\theta = 105°$ $\varphi = 90°$ or $\theta = 90°$ $\varphi = 345°$, the RCS reduction is less effective, which is the results of the bend direction of the S-type air inlet.

1. INTRODUCTION

RF stealth [1] can be regarded as the most important feature of the current fifth and coming sixth-generation fighters [2]. To be eligible as an RF stealth fighter, the radar cross section (RCS) [3] usually must be less than $-20\,$dBsm in the X band boresight direction. Due to the radar cross section reduction (RCSR) 'numbers game' [3, 274–279], a reduction in the reflections from the main scattering center is the first priority in order to achieve a low-observability military platform, either in the air or at sea. For airborne platforms, most RF stealth engineering works focus on reducing the RCS of the main scattering centers such as the slotted waveguide radar antenna, engine, vertical stabilizer, etc.. On a fighter, the engine is a major scattering source due to its all-metal isolation spoke and compressor blades [4], and many designs have therefore been proposed to reduce its RCS. Engine inlets covered with grid and coated with radar absorption materials (RAM) [5, 6] were designed for the first RF stealth aircraft, the F-117. This kind of inlet significantly hinders the air flow, and a curved S-shaped air inlet therefore became the preferred choice in later designs. Curved air inlets have attracted great academic interest over the last few decades, since in the early days they were hard to analyze analytically and were also challenging to simulate, due to their computationally resource-intensive nature. The history of research on this topic is closely related to current knowledge in electromagnetic simulation.

Crispin Jr. et al. [7] analyzed some simple square cavity shapes using a ray tracing method, and the results were consistent with earlier measurements. However, the earlier literature has tended to present RCS in units of σ/λ, which makes it difficult to compare these results with others. In his unclassified report of 1975, the legendary John Kelly outlined the basic configuration designs for low-RCS aircraft [8], in which the engine inlet was the first item discussed. An inboard inlet (attached to the fuselage) with a fuselage absorber has been found to give smaller RCS than an outboard inlet (attached to the wings), and a "plug" inlet (with cone) with an absorber can reduce the RCS by as much as 20 dB compared to

[1] Department of Electrical Engineering, National Penghu University of Science and Technology, Penghu 880, Taiwan, R.O.C.
[2] Department of Communication Engineering, Oriental Institute of Technology, Taipei 220, Taiwan, R.O.C.

an open cylinder inlet of the same size. In the 1980s, the method of moment (MoM) was developed, and Umashankar et al. [9] were able to use this approach to calculate the scattering from a simple sphere and cylinder of a lossy dielectric substance. Chou and Lee [10] calculated the modes inside a circular waveguide with multiple dielectric coatings, and found that the attenuation constant of this structure could increase by as much as 20 dB over a distance 2λ.

Ling et al. [11] developed shooting and bouncing rays (SBR) method to calculate the RCS of an arbitrarily shaped cavity, and compared the results with the modal expansion method. Graglia et al. [12] presented scattering results for both isotropic and anisotropic spherical scatterers using the MoM. Penno et al. [13] used a hybrid iterative method (HIM) that utilized an initial approximation of the surface currents on the cube faces; these currents were then inserted into the magnetic-field integral equation (MFIE) to produce improved or updated approximations of the surface currents, and this process was repeated until convergence was reached. These surface currents were then used to find the bistatic RCS for a cube with an edge length of several λ. This algorithm is still used today in several commercial RCS simulation codes. Ruan and Feng [14] used a complex ray expansion to calculate the RCS for hollow pipe targets with large apertures, similar to a realistic curved engine inlet, and found that the boresight bistatic RCS varied between -4 and -16 dBsm at $\lambda = 3.2$ cm (9.375 GHz). This algorithm is also used in current commercial RCS simulation software, and is called SBR or Ray Launching Geometrical Optics (RL-GO). Mendes and Arms [15] used a set of expansion functions to solve Maxwell's equation with Gallerkin's technique. These expansion functions were obtained by dividing the cross-section into a number of triangular patches and defining a basis function for each node in the mesh of triangles. This basis function has the desirable property of being divergence free for all the internal nodes, and surface charges are associated only with the external nodes. The RCS of a dielectric cylinder can then be computed from these surface charges. The principles underlying this approach are also used in current RCS simulation codes.

Hower et al. [16] studied the inaccuracies in the MoM and carried out a finite-difference time-domain (FDTD) [17] calculation of a non-conducting hollow sphere, and found that the inaccuracies were the result of resonance, which we understand today is the consequence of surface wave resonance. Colak et al. [18, 19] used a Bessel function expansion to calculate the bistatic RCS of a cavity-backed aperture formed from a slotted infinite circular cylinder coated with absorbing material. Rius et al. [20] tackled the engine inlet problem by separating it into stepped waveguide sections; they used an iterative technique and image theory to find the modes on both sides, and calculated the RCS due to the interior irradiation using a Kirchhoff-based aperture integral. Anastassiu et al. [21, 22] studied the bistatic RCS of an engine inlet model with a mode-matching (MM) technique, although the inlet used was simply a cylinder with some blades. The bistatic RCS obtained at 10 GHz varied between approximately -10 and -15 dBsm in the nose direction.

Odendaal and Grygier [23] presented the results of compact range RCS measurements for an inlet that was fairly realistic, although a little short (992 mm), using an engine model suitable for a UAV. The nose direction RCS at 6–12 GHz was around -10 to -30 dBsm. A time domain reflection signal similar to a modern high-resolution cross-range radar imaging technique was also presented. Hestilow [24] derived closed-form formulas for the arithmetically averaged RCS of a perfectly conducting cylinder and a perfectly conducting rectangular plate. Mackay used an SBR method to calculate the RCS of a curved inlet [25] and a straight duct [26]. Although it is fast when only a single reflection is considered, the SBR algorithm does not take into consideration the effects of surface waves reflected at the edge. Liu et al. [27] used a finite element-boundary integral (FE-BI) method to calculate the RCS of a relatively realistic duct terminated by an array of straight blades in the S and X bands. The memory required was less than 2 GB with 15 million unknowns. Due to the level of computer technology available at that time, it could be expected that the nose RCS would be somewhat different from the measurements due to the mesh number. Anastassiu [28] reviewed the algorithms used to analyze the inlet RCS problem before 2003, and cataloged 153 references according to the methods used. Wong et al. [29, 30] measured the RCS of an inlet engine mock-up in the X band, although a straight tube was used as an inlet, which misses the point. Burkholder and Lundin [31] described a forward-backward iterative physical optics algorithm for calculating the RCS of an open cavity. Chan et al. [32] measured the X band RCS of an S-shaped square inlet with 30 metal blades screwed onto the end, and simulated the RCS using an MM technique with each section assumed square waveguide modes. Fair to good agreement

was achieved between the simulation and measurements. Poyatos-Martínez et al. [33] measured the RCS of an engine mock-up with eight rotatable blades, and produced a one-dimensional high resolution range profile (HRRP) figure for their engine mock-up. Van der Ven and Schippers [34] also provided an HRRP for a civilian jet engine inlet, and reported the CPU time and memory required for the simulation. Miacci and Rezende [35] discussed the basic effects of radar absorption materials (RAM) on radar cross section reduction (RCSR) for simple and complex targets. Wang et al. [36] studied the RCS of a curved inlet using an iterative physical optics method. Mo et al. [37] simulated the RCS of a fighter head equipped with two inlets using a MoM algorithm and a highorder basis function (HOB). The results showed that the RCS for the inlet with the fighter head was much larger than for the inlets alone. Kim et al. [38] used corrugations to reduce the RCS of a straight inlet, and performed simulations based on an MM technique. Vogel [39] presented the RCS for a fighter with an engine inlet including fan blades using a multi-level fast multipole method (MLFMM) [40], and compared the results from physical optics (PO), large element-physical optics (LE-PO), and MLFMM. Ai et al. [41] wrote a book called *S-bend Stealth Inlet* which discussed aerodynamic simulations of multiple-turn S-shaped inlets, wind tunnel tests, infrared signatures, and the various algorithms used to calculate the RCS. Detailed RCS measurements and a two-dimensional range profile for a specific inlet were also presented.

Although there have been numerous studies that have calculated the RCS of an inlet in the past, we feel that they are neither clear nor accurate enough to describe the efficacy of RCSR of an inlet on an engine. In this paper, we aim to illustrate the effects of RCSR on an inlet of a fighter engine using MLFMM simulations. A digital model of an engine that is much more realistic than previous efforts is constructed and front bistatic RCS simulated, and a specific S-shaped inlet is then placed in front of the engine to demonstrate the efficacy of RCSR. Section 2 describes the definition and meaning of RCS. Section 3 describes the CAD models used and the environment of the simulation. Section 4 reports the results of the bistatic RCS simulations. Section 5 summarizes the simulation resources, and Section 6 presents the conclusion.

2. DEFINITION AND MEANING OF THE RADAR CROSS SECTION

The RCS is the ratio of scattered energy to incoming energy, as shown in Equation (1):

$$\sigma = \lim_{R \to \infty} 4\pi R^2 \frac{|E_s|^2}{|E_i|^2} \tag{1}$$

where σ is the radar cross section, E_s the scattered electric field, E_i the incoming electric field, and R the distance to the target. However, since in a real situation only the scattered waves entering enemy radar constitute a threat, a more useful definition is as follows [42]:

$$\sigma = [Geometric\_Cross\_Section] \times [Reflectivity] \times [Directivity] \tag{2}$$

Shape morphing is used to address the first and last terms of this equation, and work on RAM is mainly related to the second term. When an object is large, its RCS is generally also large, but a carefully designed object with a steep angle of incidence of the radar wave can reduce the RCS by a factor of 1000 ($-30\,\mathrm{dB}$) [43], and shape morphing is therefore the most important factor in RF stealth engineering. The scattering centers of an object can be divided into coherent and incoherent centers, as shown in Equations (3) and (4):

$$\sigma = \left| \sum_{n=1}^{N} \sqrt{\sigma_n} e^{j\phi_n} \right|^2 \tag{3}$$

$$\sigma = \sum_{n=1}^{N} \sigma_n \tag{4}$$

The distinction between these two types lies in how the scattering centers are formed. A specular reflection at the nose of an aircraft has little relationship to the reflection from the tail vertical stabilizers, while the surface waves travelling from the front edge of a wing are related to the reflection of the surface wave on the back edge of the wing. The key is the continuation of the surface waves.

The most important rule for RCS may be the 'numbers game' [3], which basically states that it is always more advantageous to reduce the RCS of the primary scattering source, and effort spent on reducing the reflections from minor scattering sources is futile.

The purpose of RF stealth is to avoid detection by enemy radar, and in this regard, the limitations on radar itself also play an important role. These limitations mainly fall into two categories: the receiver dynamic range and the system dynamic range [44]. The former is easy to understand; it originates from the circuit design and craftsmanship of the receiver, and is the range between the receiver sensitivity and the point of distortion, which is usually around 40 dB. The latter is related to RCS. In order to increase the strength of the signal returned from an RF stealth target, the output peak power of the radar needs to be increased, but this causes distortion in the output waveform, increased interference in the receiver circuit, and an increase in heat load. The system dynamic range can be expressed as:

$$D = \frac{P_{r-\max}}{P_{r-\min}} = \frac{\sigma_{\max} \cdot R_{\max}^4}{\sigma_{\min} \cdot R_{\min}^4} \tag{5}$$

where $P_{r-\max}$ and $P_{r-\min}$ are the maximum and minimum received power, respectively; $\sigma_{\max}$ and $\sigma_{\min}$ are the maximum and minimum RCS, respectively; and $R_{\max}$ and $R_{\min}$ are the maximum and minimum detection ranges, respectively. D obviously depends on the power of the radar and the intended target RCS, and is usually around 80 dB in typical situations. This equation tells us that the RCS of an RF stealth target does not need to be very small: stealth is in the eye of the beholder.

3. DIGITAL MOCKUP OF THE ENGINE AND SIMULATION SETUP

3.1. Digital Mockup of the Engine

A CAD file for a true fighter engine is fairly complicated, and for RCS simulation purposes contains too many details such as the cool air vent holes on the compressor and the turbine blades; these do not have a significant effect on the overall RCS of the engine but increase the mesh number considerably, meaning that an RCS simulation is not possible on ordinary workstation. We therefore construct a digital mockup of a fighter engine, modeled after the US F-119 engine, with radius 60 cm and length 416 cm, and in more detail than in previous studies in the academic literature. It has four vector thrust plates of length 120 cm, and all parts are assumed to be perfect conductors. Fig. 1 shows the YZ plane and the isometric view of this mockup. It has an isolation spoke with 18 blades and a center cone, and three layers of compressor blades. These blades are all tilted at $45°$, and are rotated on the Z-axis at $15°$ to each other, so that when viewed from the front, no seam can be seen but metals. The combustion chambers and two layers of turbines are located behind the blades, followed by the isolation spoke. The total number of parts is 719. Although the view from the back appears to be all metal, there is in fact a space that can allow an electromagnetic wave to pass through [45]. At the end of the engine are the four vector thrust plates with a fully open position. The boresight RCS for this mockup using FDTD simulation was reported in [45] and [46], and for the sake of completeness, we will report its RCS using an MLFMM simulation here.

3.2. Engine Inlet

Figure 2 shows a CAD model of an engine inlet obtained from the internet, taken from a CAD model of an advanced fighter. Fig. 2(a) shows the top view (XY plane) of the air inlet, and Fig. 2(b) shows the left side view (XZ plane) of the inlet, where the air enters from the right. Fig. 2(c) shows the XY plane cut view when the engine and inlet are connected together. Fig. 3(a) shows the top view of the engine and inlet inserted into a modern fighter CAD model. The engine and inlet are cut certain length in order to insert into the fighter model. Fig. 3(b) shows the three YZ plane nearfields, one XY plane near field and one XZ plane near field in the simulation. Radar wave is incident at boresight X axis direction in this figure. The blue arrow is the radar wave incident direction, and red arrow is the wave polarization direction. The inset shows the far field sphere. Fig. 3(c) shows the XY plane near field plot of Inlet+Engine at 10 GHz. Fig. 3(d) is the illustration of the difference between standard MoM and MLFMM.
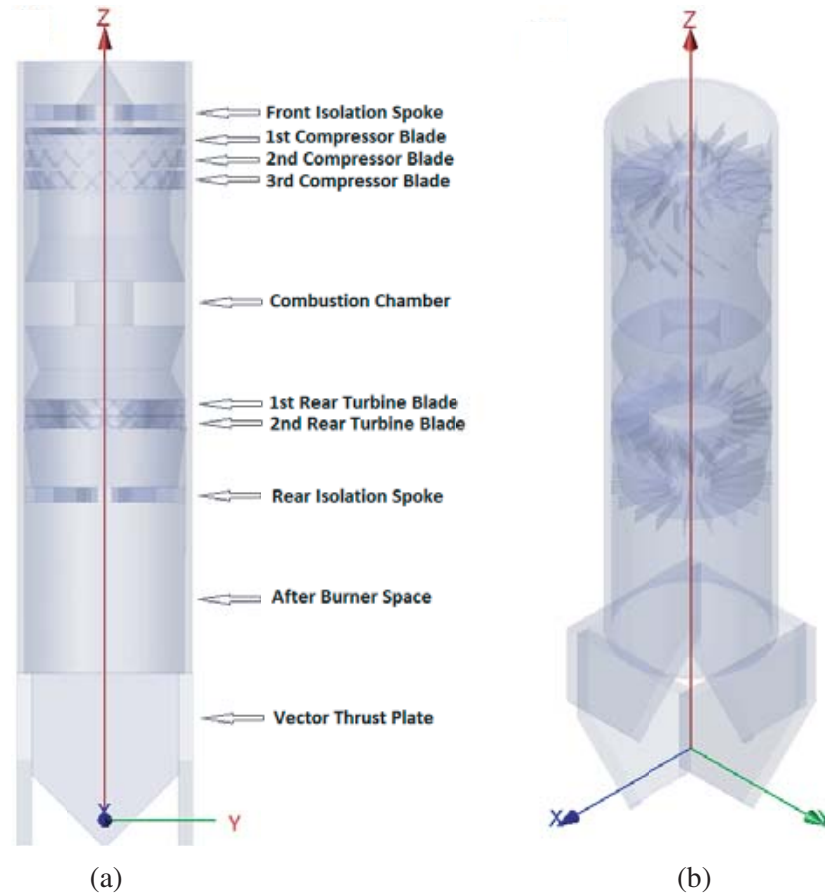
Figure 1. (a) YZ plane view of the engine digital mockup; (b) isometric view. The radius is 60 cm and the length is 416 cm (536 cm with the vector thrust plates).

3.3. Characteristics and Environment of the Simulation Algorithm

There are currently several commercially available RCS simulation codes [47], and they can be roughly divided into three categories: finite element method (FEM) [48], FDTD [49], and MoM (and its improvement, MLFMM). FEM is more suitable when inhomogeneous dielectric materials are involved, but is not very efficient when there is a large proportion of components with the same physical properties, such as metal. FDTD computes the sub-domains progressively in the Yee matrix, and since the Yee matrix has stringent restrictions in terms of time and space, the mesh number tends to become large when the RCS of an electrically large object is simulated. Fortunately, FDTD is easy to simulate in parallel, and recent advancements in GPU technology can be used to accelerate these simulations considerably. Depending on the machine architecture, an acceleration of $5 \sim 6$ times is sometimes possible. MoM solves the Maxwell equations in integral form, but the matrix is too large to be useful in the RCS simulation of electrically large objects. MLFMM basically turns the large matrix into several layers of smaller matrices, thus reducing the memory required, meaning that RCS simulation of electrically large objects is possible on a small work station. Frequency domain codes such as MLFMM also have another advantage in that the triangle size can be more flexible than FDTD; thus, in a large metal structure, the triangles tend to be larger than those near the interface or edges, which reduces the number of triangles considerably. However, MLFMM requires two sets of basis functions for each triangle when describing a dielectric medium, and the memory requirements are therefore much larger when dealing with a dielectric medium. In addition, no convergence is sometimes encountered in MLFMM.

Nowadays, commercial RCS simulation codes are often supplied in a package that includes all of
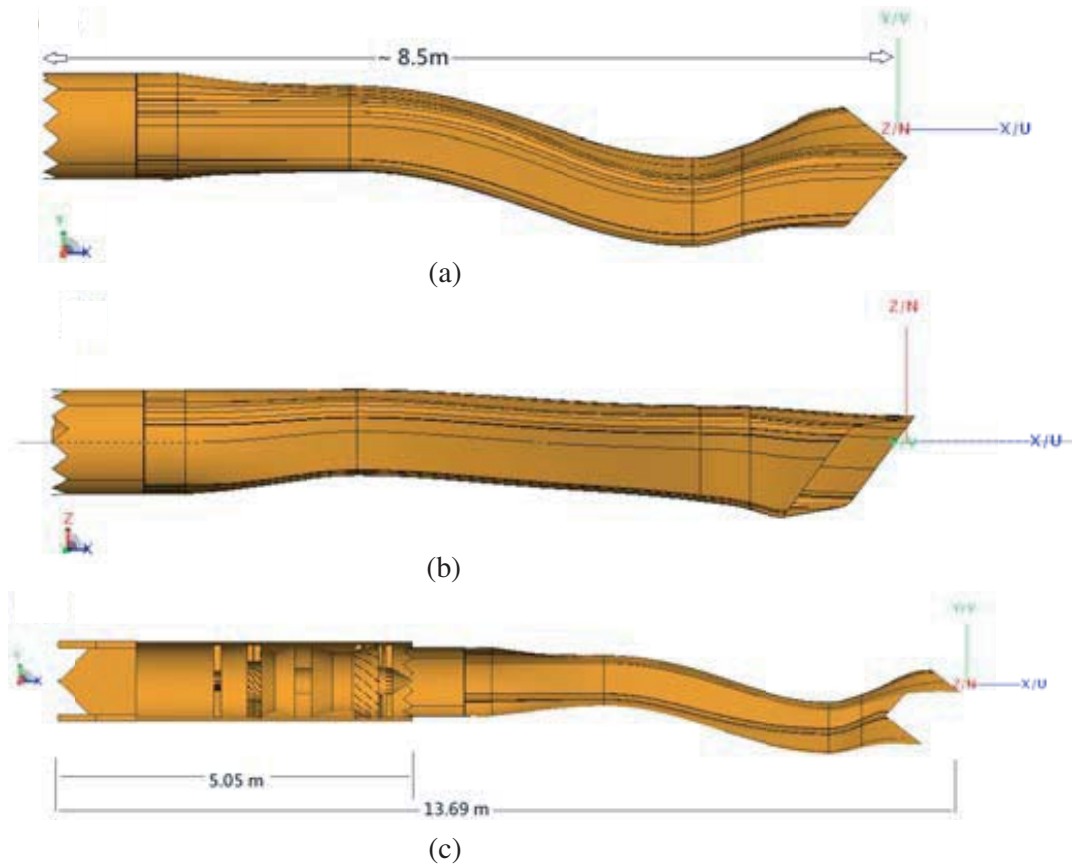
Figure 2. (a) Top view of the air inlet; (b) left side view of the inlet; (c) $Z = 0$ XY cut plane view of the inlet attached to the engine.

these main algorithms and others such as PO [50] and SBR [51] (also called RL-GO in some packages). PO is not suitable for the RCS simulation of RF stealth fighters because it cannot properly model the reflection of surface waves at the edges; although the contribution from this effect is small, because the total RCS of an RF stealth fighter is also fairly small, this effect cannot be ignored. Hence, the 'shadow radiation' concept proposed by Ufimtsev [52] plays an important role in RF stealth technology. An edge current is used in this theory to deal with the edge diffraction and to calculate the field on the other side.
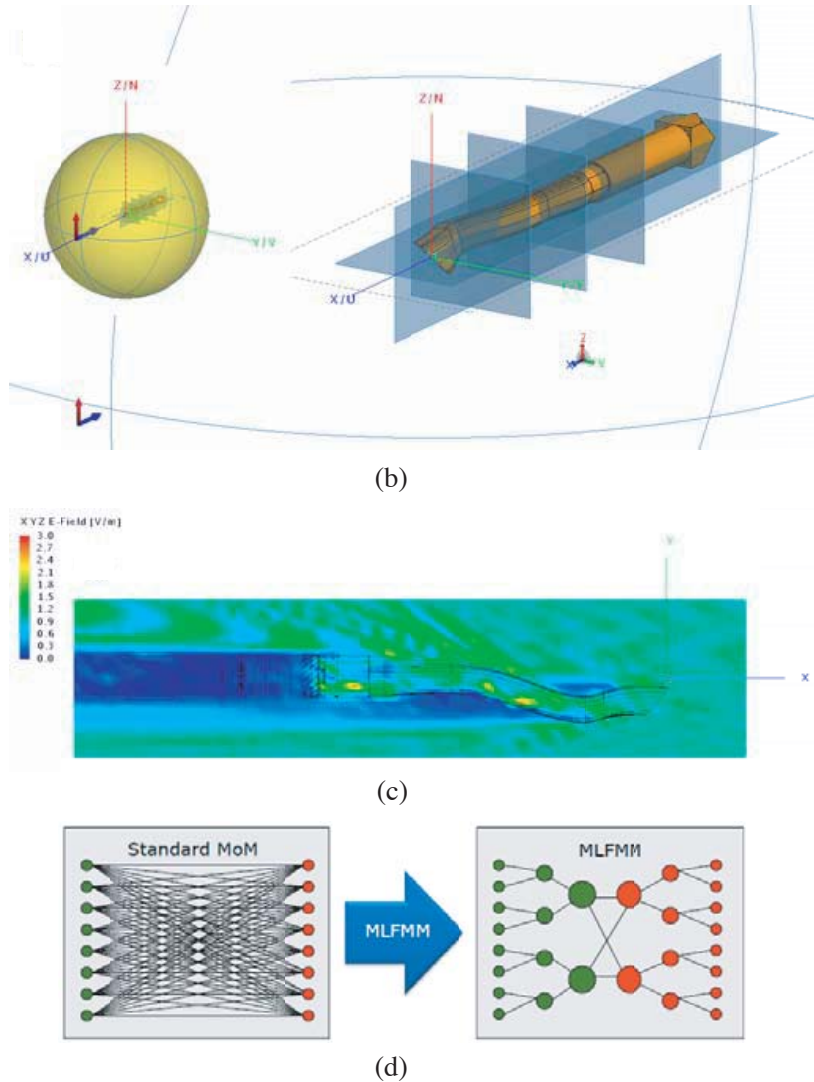

(a)

(b)

(c)

(d)
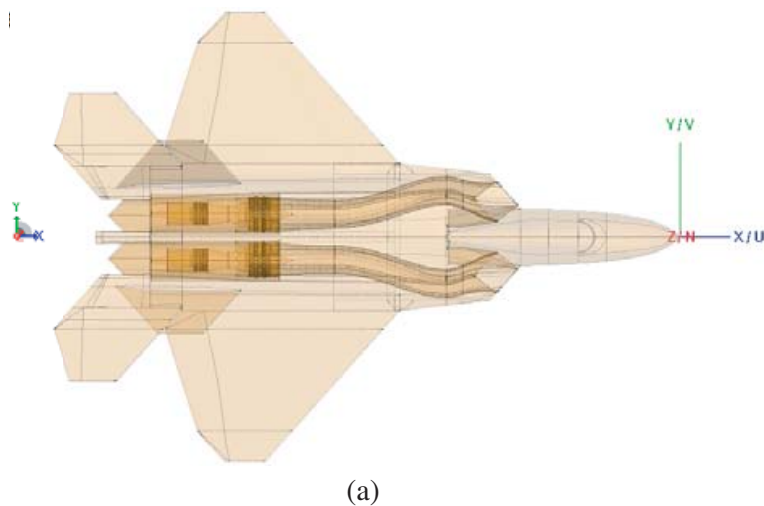
Figure 3. (a) Top view of the engine and inlet inserted into a modern fighter CAD model. The engine and inlet are cut certain length in order to insert into the fighter model. (b) The three YZ plane nearfields, one XY plane near field, and one XZ plane near field in the simulation. Radar wave is incident at boresight X axis direction in this figure, blue arrow is the radar wave incident direction and red arrow is the wave polarization direction. The inset shows the far field sphere. (c) The XY plane near field plot of Inlet+Engine at 10 GHz. (d) Illustration of the difference between standard MoM and MLFMM.

The SBR method is usually considered to be much faster than FDTD or MLFMM, but in reality, when multiple reflections are considered (such as between the blades of the engine compressor), it becomes relatively slow and does not take into consideration the edge reflections of the surface waves. However, a company has recently developed an ingenious way to get around this disadvantage by 'patching' the edge currents generated from the SBR results, and this edge current is used to regenerate new rays with a certain level of fidelity.

Thus, for RF stealth engineering purposes, FDTD and MLFMM are the two main full-wave methods that give sufficiently accurate results, and they each represent the time and frequency domains. RCS analysis in the time domain has an intrinsic advantage over the frequency domain, since the real radar signal is a time domain waveform that contains a range of frequencies; a time domain RCS simulation with the real radar waveform can therefore provide a more realistic response. However, since it contains several frequencies, it cannot reveal the resonant feature of each part as effectively as the frequency

domain code, which simulates only one frequency at a time. Multiple simulations in different frequencies are required to carry out an inverse Fourier transform into the time domain, and this is incredibly computation-intensive.

In this article, the software used was FEKO [53], and the algorithm chosen was MLFMM. Most simulations were carried out on a Supermicro 7048 server with two Intel(R) Xeon(R) CPU E5-2640v4@2.40 GHz and 512 GB memory. The E5-2640v4@2.40 GHz was a 10-core CPU (20 threads) with CPU benchmark at 15331.

3.4. Theory of MLFMM and Its Advantages in Inlet+Engine RCS Analysis

Because we use MLFMM in this article, here we explain in some detail the theory of MLFMM and its application advantages in Inlet+Engine RCS analysis. To begin with, the Maxwell's equation can be written in integral and difference forms [54], and written into matrix form [55] will greatly facilitate using computers to solve it. MoM method is a rigorous, full-wave numerical technique for solving open boundary electromagnetic problems [56]. After we write the Maxwell's equation in integral form, and discretizing the computational domain using a proper meshing scheme, the original functional equation is reduced to a set of discretized linear algebraic equations over elementary cells, and the unknown quantities are found by solving this system of linear equations. In a simplified form, the problem is reduced to the following:

$$[Z] * [I] = [V] \tag{6}$$

where $[Z]$ is called the impedance matrix; $[I]$ is the basis function matrix that contains unknown variables; and $[V]$ is the excitation matrix. Then solving the electromagnetic scattering problem becomes a matrix calculation:

$$[I] = [Z]^{-1} * [V] \tag{7}$$

A more detailed discussion can be found in [57]. So far everything is rigorous, but in practice MoM encounters great difficulty when solving electrically large object scattering problems because the matrixes become very large. MLFMM solved this issue by reducing the large matrix into layers of smaller matrix calculation as illustrated in Fig. 3(d). The advantages are: The MoM treats each N basis function in isolation, thus resulting in an N^2 scaling of memory requirements and N^3 in CPU-time. On the other hand, MLFMM formulation results in $N\log(N)$ scaling in memory and $N\log(N)^2$ in computing time. However, these two scaling relationships are theoretical, and actual saving has a lot to do with the sophistication of the code. The real advantages of MLFMM over MoM in Inlet+Engine bistatic RCS simulation using the 20 processes machine we have are listed in Table 1. The memory saving is humongous, thus making the simulation possible. Table 2 lists the actual MLFMM levels, total computing time, and peak memory usage in the two cases.

Table 1. Comparison of memory requirement of MoM and MLFMM in Inlet+Engine bistatic RCS simulation.

Cases	No. of Triangles (N)	MoM	MLFMM
Inlet+Engine 3 GHz	2740233	128.98 TB/process	26.18 GB/process
Inlet+Engine 10 GHz	13442492	3030.204 TB/process	103.87 GB/process

Table 2. MLFMM statistics in Inlet+Engine bistatic RCS simulation.

Cases	No. of Levels	Top Level of MLFMM	Total Time in Hours	Peak Memory Usage
Inlet+Engine 3 GHz	10	5	9.159	184.262 GB
Inlet+Engine 10 GHz	11	4	25.252	355.042 GB

4. RESULTS OF BISTATIC RCS SIMULATION

Since we are mainly interested in the RCS of a fighter flying above the ocean surface, radar wave polarization was set to vertical polarization (Z axis) only in the following simulations. Horizontal polarization causes a stronger clutter reflection from the ocean surface, and thus vertical polarization is usually preferred. For simplicity, the radar wave is assumed to originate from the boresight (X axis) and two other directions 15° off boresight. Only bistatic RCS is presented for we consider that bistatic RCS can reveal more precisely the nature of propagation and reflection. Monostatic RCS involves some averaging of neighboring bin RCS. Modern military radars mainly use S-band for long-range surveillance and X-band for short-range fire control, so we only present the results for these bands here.

Since the engine and air inlet are enclosed inside the fuselage, it would have been ideal if we could have simulated the entire fighter model, but unfortunately this was not possible with the available resources, and this confuses the purpose. The purpose of this article is to evaluate the efficacy of the S-shaped air inlet on the RCS reduction of the engine. Since the RCS of a fighter is composed of the three parts: the airplane, the air inlet, and the engine, if we simulate the whole airplane the efficacy of the inlet is mixed with the airplane. So we compare the RCS of the engine and the inlet only, and since the inlet and engine are enclosed inside the airplane, we think that only the ±30° regions along the boresight direction is of relevance. We mark the regions with two purple lines.

4.1. Boresight Bistatic RCS of the Engine

Figure 4(a) shows the bistatic XZ cut RCS of the engine model at 2 GHz (blue), 3 GHz (green), and 4 GHz (red). The maximum value in the boresight direction is 19.2078 dBsm at 2 GHz, 25.5728 dBsm at 3 GHz, and 28.1133 dBsm at 4 GHz. Fig. 4(b) shows the bistatic XY cut RCS of the engine model in the S band. The blue line represents 2 GHz, the green line 3 GHz, and the red line 4 GHz. Because the engine is a symmetrical CAD model, the maximum value in the boresight direction at these three frequencies are close to the XZ cut.

Figure 4(c) shows the bistatic XZ cut RCS of the engine model in the X band. The blue line represents 8 GHz, the green line 10 GHz, and the red line 12 GHz. The maximum value in the boresight direction is 25.6934 dBsm at 8 GHz, 30.3913 dBsm at 10 GHz, and 39.0614 dBsm at 12 GHz. Fig. 4(d) shows the bistatic XY cut RCS, and the maximum values at boresight direction are close to the XZ cut RCS.

The general trend is that as frequency increases, the front boresight bistatic RCS increases. As the frequency increases from the S to X band, the front boresight bistatic RCS increases considerably. From these two figures, we can see that the bistatic boresight RCS of the engine alone is fairly large, close to 40 dBsm which is almost as large as that of a small ship.

4.2. Boresight Bistatic RCS of the Air Inlet

Figure 5(a) shows the bistatic XZ cut RCS of the air inlet model in the S band, where the blue, green, and red lines represent 2, 3, and 4 GHz. The maximum value in the boresight direction is −2.34889 dBsm at 2 GHz, and this quickly drops to −23.5636 dBsm at 3 GHz and −19.4932 dBsm at 4 GHz. Fig. 5(b) shows the bistatic XY cut RCS, with the same color coding as above. A similar trend is seen as in the XZ cut case. The much larger boresight bistatic RCS at 2 GHz may be due to a resonance effect between the wave and the entire inlet, and due to the steep drop in the RCS from 2 to 3 GHz, this air inlet is effectively producing a small RCS in the boresight direction, which becomes more obvious in the X band.

Figure 5(c) shows the bistatic XZ cut RCS of the air inlet model in the X band, where the blue, green, and red lines indicate 8, 10, and 12 GHz. The boresight direction RCS is −25.2985 dBsm at 8 GHz, −33.0166 dBsm at 10 GHz, and −28.3865 at 12 GHz. Fig. 5(d) shows the bistatic XY cut RCS, with the same color coding as the XZ case. The values for the boresight bistatic RCS in Figs. 5(c) and 5(d) are all well below −20 dBsm, which is a common criterion for RF stealth.
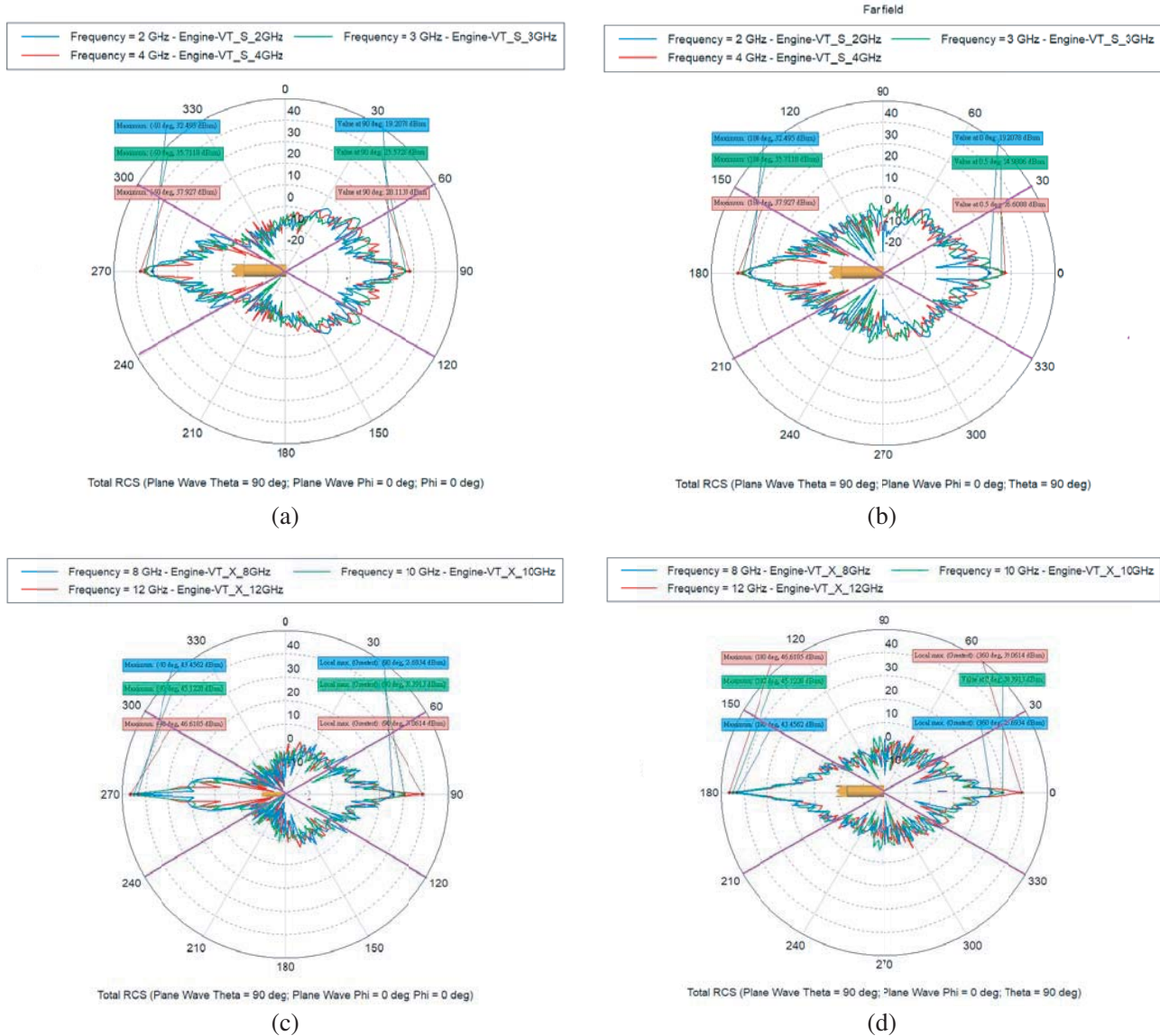
(a)

(b)

(c)

(d)

Figure 4. Bistatic RCS of the engine model. (a) The XZ cut RCS in S-band. The blue, green, and red lines indicates 2, 3, and 4 GHz. The maximum value in the boresight direction is 28.1133 dBsm at 4 GHz. (b) The XY cut RCS in S-band. The blue, green, and red lines indicates 2, 3, and 4 GHz. The maximum value in the boresight direction is 26.6088 dBsm at 4 GHz. (c) The XZ cut RCS in X-band. The blue, green, and red lines indicates 8, 10, and 12 GHz. The maximum value in the boresight direction is 39.0614 dBsm at 12 GHz. (d) The XY cut RCS in X-band. The blue, green, and red lines indicates 8, 10, and 12 GHz. The maximum value in the boresight direction is 39.0614 dBsm at 12 GHz.

4.3. Comparison of Bistatic RCS for the Engine, Air Inlet, and Air Inlet+Engine Models When Radar Wave Is Incident from Boresight Direction

In this section we examine the bistatic RCS of the engine and air inlet connected together, and compare it with engine and inlet alone when the radar wave is incident from boresight direction.

Figure 6(a) shows a comparison of the XZ cut bistatic RCS of the engine (blue), inlet (green), and inlet+engine (red) at 3 GHz. At boresight direction, the bistatic RCS for engine is 25.2181 dBsm, for inlet is -23.5635 dBsm, and for inlet+engine is 14.2635 dBsm. We can see the inlet effective masks the
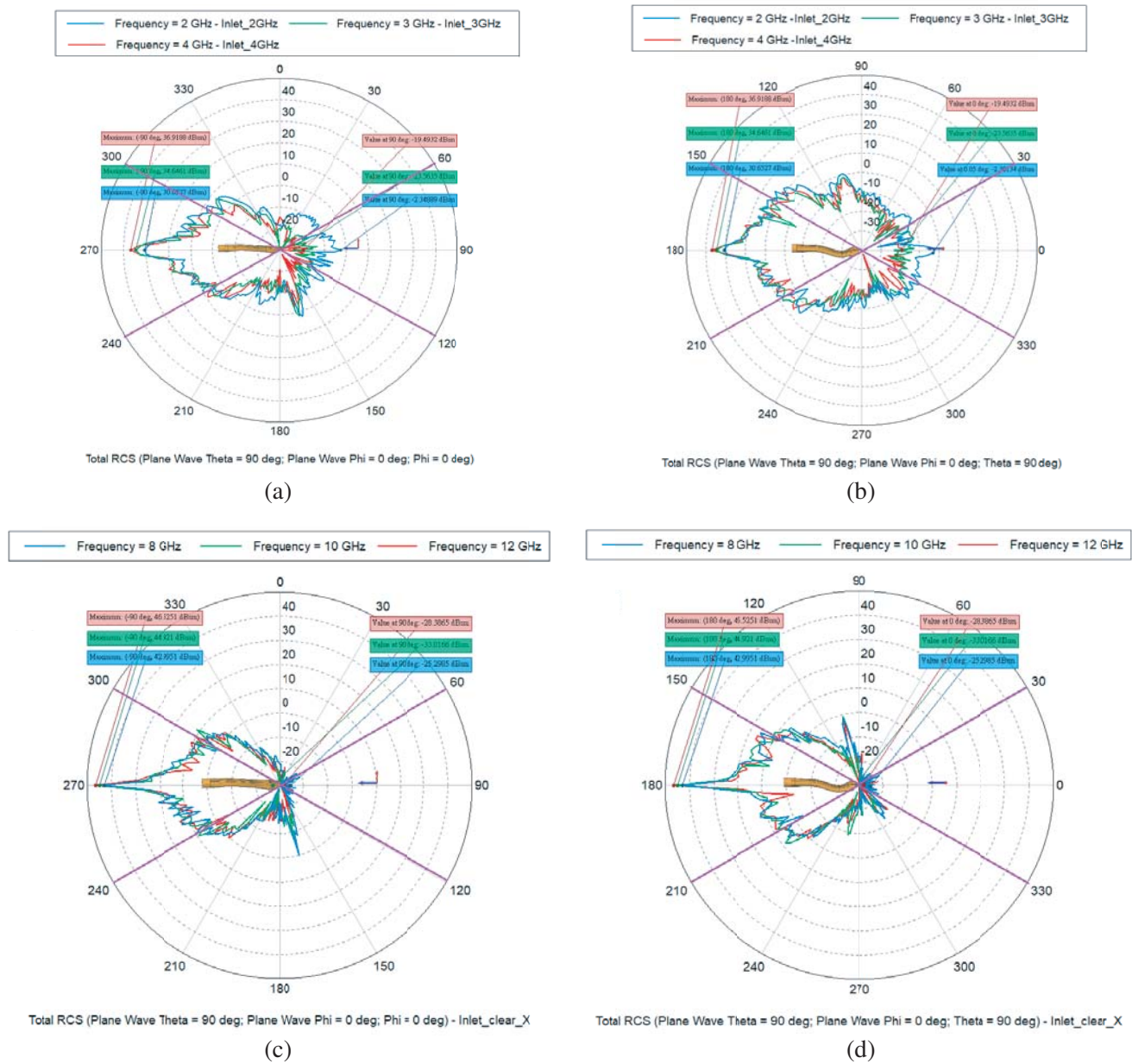
(a)

(b)

(c)

(d)

Figure 5. Bistatic RCS of the inlet model. (a) The XZ cut RCS in S-band. The blue, green, and red lines indicate 2, 3, and 4 GHz. The boresight RCS is -2.34889 dBsm at 2 GHz, and this quickly drops to -23.5636 dBsm at 3 GHz and -19.4932 dBsm at 4 GHz. (b) The XY cut RCS in S-band. The blue, green, and red lines indicates 2, 3, and 4 GHz. The boresight RCS decrease the same extent as the XZ plane. (c) The XZ cut RCS in X-band. The blue, green, and red lines indicates 8, 10, and 12 GHz. The boresight RCS at these frequencies are -25.2985, -33.0166, and -28.3865 dBsm. (d) The XY cut RCS in X-band. The blue, green, and red lines indicates 8, 10, and 12 GHz. The boresight RCS decrease the same extent as the XZ plane.

large bistatic RCS of the engine, and reduces the engine RCS by 10.9549 dBsm. Fig. 6(b) shows the bistatic XY cut RCS at 3 GHz, and the boresight bistatic RCS for the three items. The trend is similar to the Fig. 6(a) case with engine RCS reduces by 12.9315 dBsm.

Figure 6(c) shows the bistatic XZ cut RCS at 10 GHz. At boresight direction, the bistatic RCS for the engine is 28.0553 dBsm, for the inlet is -32.8289 dBsm, and for inlet+engine is 11.9917 dBsm.
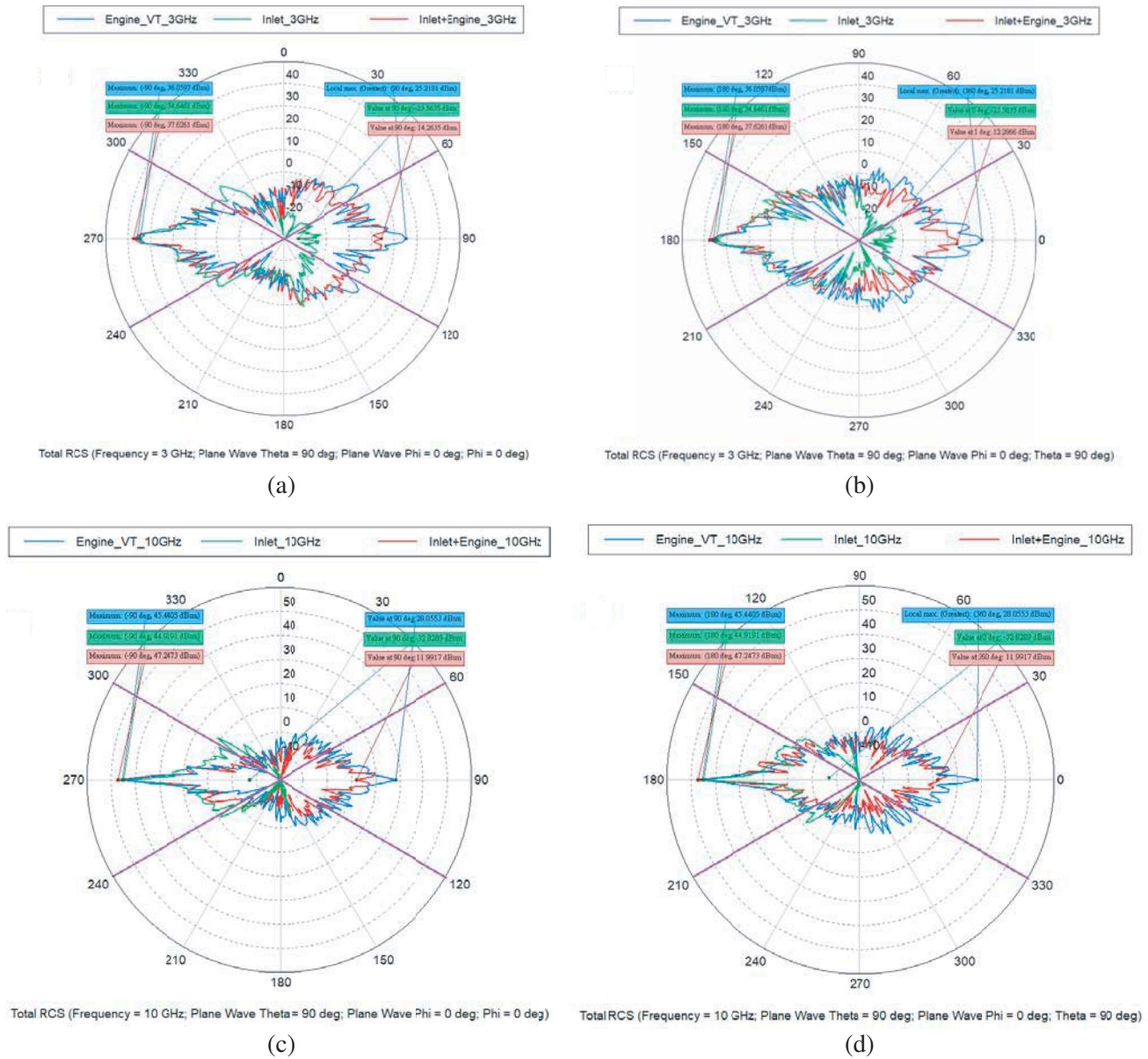
(a)

(b)

(c)

(d)

Figure 6. Comparison of the boresight RCS for the engine (blue), inlet (green), and inlet+engine (red). (a) XZ plane at 3 GHz. The boresight RCS for engine is 25.2181 dBsm, for inlet is -23.5635 dBsm, for inlet+engine is 14.2635 dBsm. (b) XY plane at 3 GHz. The boresight RCS for engine is 25.2181 dBsm, for inlet is -23.5635 dBsm, for inlet+engine is 12.2866 dBsm. (c) XZ plane at 10 GHz. The boresight RCS for engine is 28.0553 dBsm, for inlet is -32.8289 dBsm, for inlet+engine is 11.9917 dBsm. (d) XY plane at 10 GHz. The boresight RCS for these three are the same as in XZ plane.

The inlet reduces engine RCS by 16.0636 dBsm. Fig. 6(d) shows the bistatic XY cut RCS at 10 GHz with the same color coding. The boresight bistatic RCS values of the three items are roughly the same and the RCS reduction value is the same.

From these comparisons, we can see that the inlet does considerably reduce the boresight bistatic RCS of the engine, although the effects are not as good as one imagined. The resultant bistatic RCS is much larger than the inlet alone. The reason for this may be that the radar waves reflected from the engine can still somehow reflected back to the radar through multiple reflections inside the inlet.

4.4. Comparison of Bistatic RCS for the Engine, Air Inlet, and Inlet+Engine Models When Radar Wave Is Incident from $\theta = 105°$, $\phi = 0°$ Direction

In this section we examine the bistatic RCS when the radar wave is incident from 15 below boresight direction, which will resemble a ground based radar.

Figure 7(a) shows the bistatic XZ cut RCS for engine (blue), inlet (green), and inlet+engine (red)
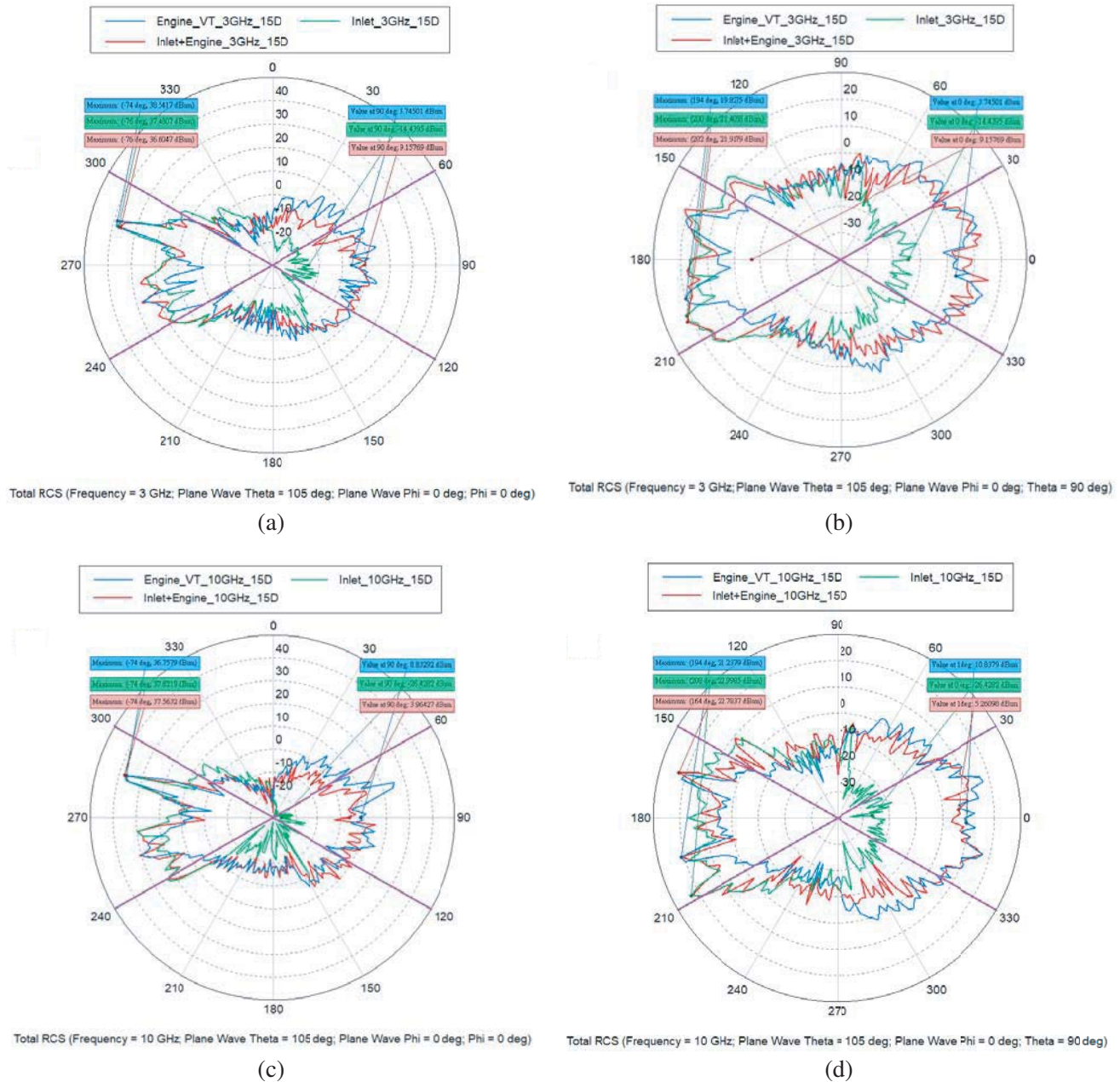

(a)

(b)

(c)

(d)

Figure 7. Comparison of the bistatic RCS when radar wave is incident from $\theta = 105°$, $\phi = 0°$ direction for the engine (blue), inlet (green), and inlet+engine (red). (a) XZ plane at 3 GHz. The boresight RCS for engine, inlet, and inlet+engine are 3.74501, -14.4395, and 9.15769 dBsm. (b) XY plane at 3 GHz. (c) XZ plane at 10 GHz. The boresight RCS for engine, inlet, and inlet+engine are 8.83292, -26.4282, and 3.96427 dBsm. (d) XY plane at 10 GHz. The boresight RCS for engine, inlet, and inlet+engine are 10.8379, -26.4282, and 5.26098 dBsm.

at 3 GHz. The front bistatic RCS for engine is 3.74501 dBsm, for inlet is -14.4395 dBsm, and for inlet+engine is 9.15769 dBsm. The inlet does not reduce engine RCS in this case, instead increases 5.41718 dBsm. Fig. 7(b) shows the bistatic XY cut RCS of the same three items. The front bistatic RCS is about the same as in Fig. 7(a).

Figure 7(c) shows the bistatic XZ cut RCS for engine (blue), inlet (green), and inlet+engine (red) at 10 GHz. The front bistatic RCS for engine is 8.83292 dBsm, for inlet is -26.4282 dBsm, and for inlet+engine is 3.96427 dBsm. The inlet reduces the engine RCS by 5.1965 dBsm. Fig. 7(d) shows
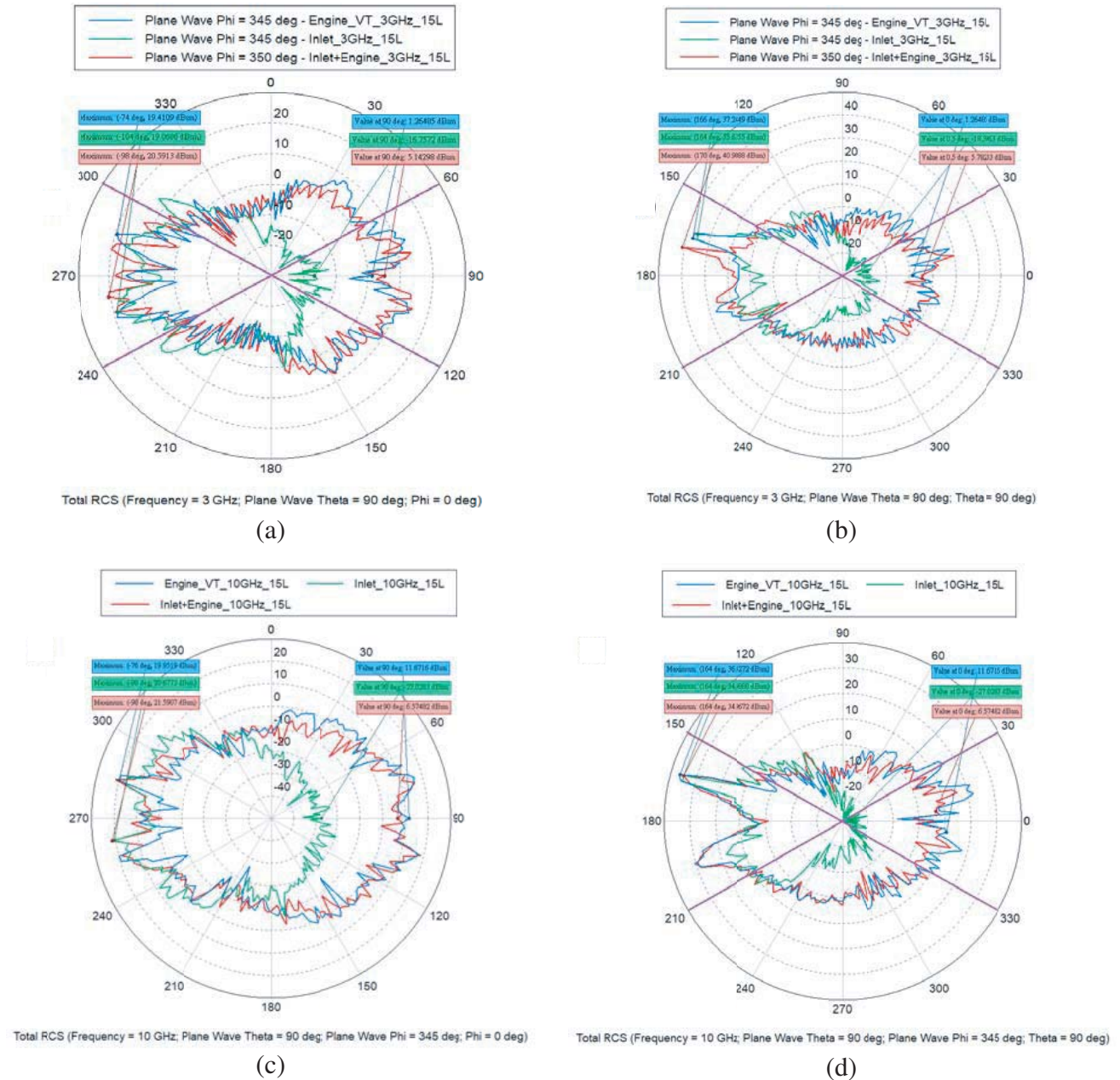

Figure 8. Comparison of the bistatic RCS when radar wave is incident from $\theta = 90°$, $\phi = 345°$ direction for the engine (blue), inlet (green), and inlet+engine (red). (a) XZ plane at 3 GHz. The boresight RCS for engine, inlet, and inlet+engine are 1.26485, -16.7572, and 5.78233 dBsm. (b) XY plane at 3 GHz. (c) XZ plane at 10 GHz. The boresight RCS for engine, inlet, and inlet+engine are 11.6716, -27.0283, and 6.57482 dBsm. (d) XY plane at 10 GHz.

the bistatic XY cut RCS for engine (blue), inlet (green), and inlet+engine (red) at 10 GHz. The front bistatic RCS for engine is 10.8379 dBsm, for inlet is -26.4282 dBsm, and for inlet+engine is 5.26098 dBsm. The inlet reduces the engine RCS by 5.5771 dBsm.

4.5. Comparison of Bistatic RCS for the Engine, Air Inlet, and Inlet+Engine Models When Radar Wave Is Incident from $\theta = 90°$, $\phi = 345°$ Direction

In this section we examine the bistatic RCS when the radar wave is incident from $\pm 15°$ right of the boresight direction. Since the inlet model we simulate is the starboard side model, the only possible radar wave incident direction is from the starboard side.

Figure 8(a) shows the bistatic XZ cut RCS for engine (blue), inlet (green), and inlet+engine (red) at 3 GHz. The front bistatic RCS for engine is 1.26485 dBsm, for inlet is -16.7572 dBsm, and for inlet+engine is 5.14298 dBsm. The inlet increases the engine RCS by 3.87813 dBsm. Fig. 8(b) shows the bistatic XY cut RCS of the same three items. The front bistatic RCS for engine is 1.26485 dBsm, for inlet is -16.7572 dBsm, and for inlet+engine is 5.41928 dBsm. The inlet actually increases engine RCS by 4.14813 dBsm

Figure 8(c) shows the bistatic XZ cut RCS for engine (blue), inlet (green), and inlet+engine (red) at 10 GHz. The front bistatic RCS for engine is 11.6719 dBsm, for inlet is -27.0283 dBsm, and for inlet+engine is 6.57482 dBsm. The inlet reduces engine RCS by 5.09708 dBsm. Fig. 8(d) shows the bistatic XY cut RCS for engine (blue), inlet (green), and inlet+engine (red) at 10 GHz. The boresight bistatic RCS for engine is 11.6716 dBsm, for inlet is -27.0283 dBsm, and for inlet+engine is 6.57482 dBsm. The trend is the same as Fig. 8(c).

5. SIMULATION RESOURCES ANALYSIS

The resources required by a simulation are often used as a benchmark of the efficiency of the algorithm used. Here, we use the air inlet+engine at 12 GHz as an example. Table 3 gives the simulation parameters for this case. The main requirement for this simulation is the installation of DRAM memory. In this case, the simulation consumes 267.362 GB of DRAM. Besides DRAM, FEKO also requires the dynamic allocation of hard drive memory for temporary storage of up to 228.852 GB. The simulation time strongly depends on the mesh (triangle) number and the iteration convergence threshold. The use of more triangles usually means a more accurate result, but this is also related to the iteration convergence threshold. A great deal of time is spent on reaching the threshold as the convergence curve becomes flat.

Table 3. Computational resources required for 12 GHz inlet+engine simulation.

2 CPU Cores (thread)	Installed DRAM	Surface of all triangles	No. of metallic triangles	No. of metallic edges
10 cores (20 threads)	512 GB	8.18828×10^1 m^2	6594142	9893489
Maximum No. of iterations	Dynamic memory in HD	Peak memory for all processes	Time for linear equation	Total simulation time
300	228.852 GB	267.362 GB	22.089 hr	22.697 hr

6. CONCLUSION

In this article, we demonstrate how to evaluate the efficacy of an S-shaped air inlet in terms of reduction on the bistatic RCS of an engine. We use much more realistic digital markup models than in previous studies, and our approach is considerably less expensive than building a wooden model and conducting RCS measurements.

The results show that when the radar wave is coming from boresight direction (Case C), the curved S-type air inlet can reduce the engine boresight bistatic RCS by roughly $-10 \sim -12$ dBsm at 3 GHz and roughly -16 dBsm at 10 GHz. The RCS reduction effect is substantial. When the radar wave is incident from $15°$ below boresight (Case D), the inlet increases engine RCS by about 5 dBsm at 3 GHz and reduces engine RCS by about 5 dBsm at 10 GHz. When the radar wave is coming from $15°$ off boresight from the starboard side (Case E), the inlet increases the engine RCS by about 4 dBsm at 3 GHz and reduces the engine RCS by about 5 dBsm.

How to interpret the RCS results? We think the inlet works pretty well when the radar wave is incident from boresight because the inlet is designed from that assumption at the beginning. The inlet S-shape is curved to the right to block the radar wave coming directly from boresight, but when the radar waves are coming from $15°$ off boresight, the curved S-shape no longer matter, instead it is the multiple scattering that dominates the RCS.

When the inlet RCS reduction works (Case C), although these reductions are significant, the resultant RCSs of around 12 dBsm at 3 GHz and 12 dBsm at 10 GHz are still well above the commonly desired -20 dBsm for RF stealth. For this, RAM is needed to further reduce the RCS. The study on RAM effects is not included here. Generally, a well-designed RAM can reduce RCS by as much as $-10 \sim -20$ dBsm depending on the design, composition and the coating technique, and the RF stealth threshold can therefore be reached, which demonstrates RF stealth requires attention to every detail.

A question that is frequently raised about such simulations is whether the results are accurate, and this is not a simple question with a short answer. Contemporary RCS simulation software is usually accurate to within 1 dB along the boresight direction compared with certain standard shape corner reflector measurements, and some benchmark literatures exist [53, 58]. SAAB joined with Boeing a few years ago to design and build the new US trainer aircraft T-X [59] using the same RCS simulation software we use in this article, only the license fee for their cluster machine is rumored to amount to millions of US dollars. Although it is just a trainer aircraft, the rumored boresight RCS of the T-X at X band is less than $0.5 \, \mathrm{m}^2$ or -3 dBsm. With a little RAM modification, this trainer can become a fighter very soon.

When applied to realistic models, a finer mesh will always produce slightly different results, typically assumed to be 'more accurate'; however, the memory requirement and simulation time increase considerably. The theoretical memory requirement for MoM is proportional to N^2, while for MLFMM this is $N \log(N)$, where N is the mesh (triangle) number. The simulation time is mainly determined by the iteration convergence threshold. Near the end of the simulation, very long calculations are required for very little gain in accuracy. A GPU and a larger number of cores can significantly shorten the simulation time, but they are expensive. Contrary to general belief, a simulation is not always successful. Each change of frequency requires a new mesh to be generated, and this new mesh sometimes creates problems. CAD models from internet also frequently contain defects that are hard to find.

On the other hand, experimental RCS measurements are also quite challenging, and it is often not easy to obtain 'accurate' results, particularly in the realm of RF stealth. It is fairly expensive to construct an anechoic chamber that can measure down to -30 dBsm RCS with sufficient bandwidth in the S and X bands because the instrument measurement sensitivity is usually expressed by dBm/Hz, and the larger the bandwidth is, the higher the noise floor is. Nowadays new military radar bandwidth is usually quite large. To encompass a large aircraft instead of a model like frequently seen in academic literatures, the anechoic chamber is extremely expensive, usually in hundreds of millions of US dollars. That is why such chambers exist only in military facilities, and measurement results are classified and are unavailable to most academic communities.

Current direction in this field is towards whole-spectrum and all-direction RF stealth, which poses real challenges in design, simulation, and manufacturing.

ACKNOWLEDGMENT

REFERENCES

1. Lynch, Jr., D., *Introduction to RF Stealth*, SciTech, Raleigh, NC, 2004.

2. Fifth-generation jet fighters, [Online], Available: https://en.wikipedia.org/wiki/Fifth-generation_jet_fighter, last accessed 20180228.

3. Knott, E. F., M. T. Tuley, and J. F. Shaeffer, *Radar Cross Section* (Scitech Radar and Defense), 2nd Edition, SciTech, London, UK, 2004.

4. Royce, R., *The Jet Engine*, 5th Edition, Wiley, 2015.

5. Vinoy, K. J. and R. M. Jha, *Radar Absorbing Materials: From Theory to Design and Characterization*, Kluwer Academic, Boston, MA, USA, 1996.

6. Saville, P., "Review of radar absorbing materials," Technical Memorandum, Defense R&D Canada — Atlantic TM 2005-003, 2005.

7. Crispin, Jr., J. W. and A. L. Maffett, "Estimating the radar cross section of a cavity," *IEEE Trans. Aerosp. Electron. Syst.*, Vol. 6, No. 5, 672–674, Sept. 1970.

8. Kelly, J. D., "Configuration design for low RCS," Boeing Aerospace Company 2-5173-JDK-75-068, Sept. 1975.

9. Umashankar, K., A. Taflove, and S. Rao, "Electromagnetic scattering by arbitrary shaped three-dimensional homogeneous lossy dielectric objects," *IEEE Trans. Antennas Propag.*, Vol. 34, No. 6, 758–766, Jun. 1986.

10. Chou, R. C. and S. W. Lee, "Modal attenuation in multilayered coated waveguides," *IEEE Trans. Microw. Theory Techn.*, Vol. 36, No. 7, 1167–1176, Jul. 1988.

11. Ling, H., R.-C. Chou, and S.-W. Lee, "Shooting and bouncing rays: Calculating the RCS of an arbitrarily shaped cavity," *IEEE Trans. Antennas Propag.*, Vol. 37, No. 2, Feb. 1989.

12. Graglia, R. D., P. L. E. Uslenghi, and R. S. Zich, "Moment method with isoparametric elements for three-dimensional anisotropic scatterers," *Proc. IEEE*, Vol. 77, No. 5, 750–760, May 1989.

13. Penno, R. P., G. A. Thiele, and K. M. Pasala, "Scattering from a perfectly conducting cube," *Proc. IEEE*, Vol. 77, No. 5, 815–823, May 1989.

14. Ruan, Y. Z. and W. L. Feng, "RCS calculation of open cavities by complex ray expansion," *IEE Proc. — F*, Vol. 138, No. 5, 397–399, Oct. 1991.

15. Mendes, L. and E. Arms, "TE-scattering from dense homogeneous infinite dielectric cylinders of arbitrary cross-section," *IEEE Trans. on Magn.*, Vol. 27, No. 5, 4295–4298, Sept. 1991.

16. Hower, G. L., R. G. Olsen, J. D. Earls, and J. B. Schneider, "Inaccuracies in numerical calculation of scattering near natural frequencies of penetrable objects," *IEEE Trans. Antennas Propag.*, Vol. 41, No. 7, 982–986, Jul. 1993.

17. Gedney, S. D., *Introduction to the Finite-Difference Time Domain (FDTD) Methods for Electromagnetics*, 1st Edition, Morgan & Claypool Publishers, 2011.

18. Colak, D., A. I. Nosich, and A. Altintas, "Radar cross-section study of cylindrical cavity-backed apertures with outer or inner material coating: The case of *E*-polarization," *IEEE Trans. Antennas Propag.*, Vol. 41, No. 11, 1551–1559, Nov. 1993.

19. Colak, D., A. I. Nosich, and A. Altintas, "Radar cross-section study of cylindrical cavity-backed apertures with outer or inner material coating: The case of *H*-polarization," *IEEE Trans. Antennas Propag.*, Vol. 43, No. 5, 440–447, May 1995.

20. Rius, J. M., A. Lozano, and A. Cardama, "RCS of engine inlets by a spectral iterative technique," *23rd European Microwave Conf.*, Madrid, Spain, Sept. 1993.

21. Anastassiu, H. T., J. L. Volakis, D. C. Ross, and D. Andersh, "Electromagnetic scattering from simple jet engine models," *IEEE Trans. Antennas Propag.*, Vol. 44, No. 3, 420–421, Mar. 1996.

22. Anastassiu, H. T., "Electromagnetic scattering from jet engine inlets using analytical and fast integral equation methods," Ph.D. thesis, U. of Michigan, 1997.

23. Odendaal, J. W. and D. Grygier, "RCS measurements and results of an engine-inlet system design optimization," *IEEE Antennas and Propag. Mag.*, Vol. 42, No. 6, 16–23, Dec. 2000.

24. Hestilow, T. J., "Simple formulas for the calculation of the average physical optics RCS of a cylinder and a flat plate over a symmetric window around broadside," *IEEE Antennas and Propag. Mag.*, Vol. 42, No. 5, 48–52, Oct. 2000.

25. Mackay, A., "Random wave and Schell model for the mean RCS of bent chaotic ducts with a homogeneous scattered aperture field distribution," *IEE Proc. — Radar, Sonar Navig.*, Vol. 148, No. 6, 338–342, Dec. 2001.

26. Mackay, A., "Random wave methods for the prediction of the RCS of homogeneous chaotic straight ducts," *IEE Proc. — Radar, Sonar Navig.*, Vol. 148, No. 6, 331–337, Dec. 2001.

27. Liu, J., E. Dunn, J.-M. Jin and C. S. Liang, "Computation of radar cross section of jet engine inlets with a nonuniform cross section and complex internal structures," *Proc. of IEEE Int. Sym. Ant. and Prop.*, San Antonio, TX, USA, Aug. 2002.

28. Anastassiu, H. T., "A review of electromagnetic scattering analysis for inlets, cavities, and open ducts," *IEEE Antennas and Propag. Mag.*, Vol. 45, No. 6, 27–40, Dec. 2003.

29. Wong, S., E. Riseborough, G. Duff, and K. K. Chan, "Experimental facility for measuring aircraft inlet/engine radar cross section," *RTO-MP-SET-080*, Oslo, Norway, Oct. 11–13, 2004.

30. Wong, S. K., E. Riseborough, G. Duff, and K. K. Chan, "Radar cross-section measurements of a full-scale aircraft duct/engine structure," *IEEE Trans. Antennas Propag.*, Vol. 54, No. 8, 2436–2441, Aug. 2006.

31. Burkholder, R. J. and T. Lundin, "Forward-backward iterative physical optics algorithm for computing the RCS of open-ended cavities," *IEEE Trans. Antennas Propag.*, Vol. 53, No. 2, 793–799, Feb. 2005.

32. Chan, K. K., S. K. Wong, and E. S. Riseborough, "Radar cross section modeling and measurements of inlets and cylinders with skew blades," *IEEE Trans. Antennas Propag.*, Vol. 54, No. 10, 2930–2939, Oct. 2006.

33. Poyatos-Martínez, D., D. Escot-Bocanegra, R. Fernández-Recio, and I. Montiel-Sánchez, "RCS analysis of a configurable mock-up cavity with blade motion capability," *IEEE Trans. on Magn.*, Vol. 45, No. 3, 1096–1099, Mar. 2009.

34. Van Der Ven, H. and H. Schippers, "High range resolution profiles for a civilian aircraft inlet," *NLR-TP-2010-527*, National Aerospace Laboratory NLR, Feb. 2011.

35. Miacci, M. A. S. and M. C. Rezende, "Basics on radar cross section reduction measurements of simple and complex targets using microwave absorbers," *Applied Measurement Systems*, Z. Haq (ed.), Ch. 16, 351–376, InTech, Feb. 2012.

36. Wang, L., Y.-C. Zhong, and K.-Y. Zhang, "Electromagnetic scattering study for metal/dielectric coated inlet diffuser," *Acta Phys. Sin.*, Vol. 61, No. 23, 234101, 2012 (in Chinese).

37. Mo, J., W. Fang, H. Xue, Y. Yan, and Z. Ma, "Accurate evaluation of RCS on the structure of aircraft Inlets," *Proc. of Int. Sym. Ant. Prop. (ISAP) 2013*, Nanjing, China, Oct. 2013.

38. Kim, Y. D., H. Lim, J. H. Han, W. Y. Song, and N. H. Myung, "RCS reduction of open-ended circular waveguide cavity with corrugations using mode matching and scattering matrix analysis," *Progress In Electromagnetics Research*, Vol. 146, 57–69, 2014.

39. Vogel, M., "Radar cross section of aircraft with engine inlets including fan blades," *Proc. of Int. Sym. on Ant. Prop. (APSURSI)*, Fajardo, Puerto Rico, Jun. 26–Jul. 1, 2016.

40. Song, J., C.-C. Lu, and W. C. Chew, "Multilevel fast multipole algorithm for electromagnetic scattering by large complex objects," *IEEE Trans. Antennas Propag.*, Vol. 45, No. 10, 1488–1493, Oct. 1997.

41. Ai, J.-C., L. Chou and C.-J. Yang, *S-bend Stealth Inlet*, Defense Industry Pub., ISBN 978-7-118-11082-1, 2017 (in Chinese).

42. Naval Air Warfare Center Weapons Division, *Electronic Warfare and Radar Systems Engineering Handbook*, NAWCWD TP 8347, 4th Edition, 2013.

43. Chung, S. S. M., "Ch. 1: Manipulation of radar cross sections with plasma," *Radar Systems: Technology, Principles and Applications*, 1–44, Wen-Qin Wang (Ed.), Nova Science Pub. Inc., UK, May 17, 2013.

44. Dynamical Range of a Receiver, [Online], Available: https://www.radartutorial.eu/09.receivers/rx-52.en.html.

45. Tuan, S.-C. and S. S. M. Chung, "Radar cross section and near field of an engine digital mock-up under UHF and S band radar illumination," *EuRad2018, European Microwave Week (EuMW2018)*, Ifema Feria De Madrid, Spain, Sept. 23–28, 2018.

46. Chung, S. S. M., "Parametric simulation on reduction of S-band rear bistatic radar cross section of jet engine with vector thrust nozzle via plasmatized exhaust," *IEEE Trans. Plasma Sci.*, Vol. 45, No. 3, 388–404, Jan. 31, 2017.

47. RCS simulation software, CAST, [Online], Available: http://virtual.vtt.fi/, CST, [Online], Available: https://www.cst.com, Epsilon, [Online], Available: http://www.roke.co.uk/, EMPro, [Online], Available: http://www.keysight.com/, Efield, [Online], Available: http://www.efieldsolutions.com/, EMPIRE, [Online], Available: http://www.empire.de/, HFSS, [Online], Available: http://www.ansys.com/, FEKO, [Online], Available: https://www.feko.info/, GEMS, [Online], Available: http://www.2comu.com/, RASES, [Online], Available: http://bilgem.tubitak.gov.tr/, XFDTD, [Online], Available: http://www.remcom.com/, last accessed 20200101.

48. Strange, G. and G. Fix, *An Analysis of the Finite Element Methods*, 2nd Edition, Wellesley-Cambridge, May 2008.

49. Gedney, S., *Introduction to the Finite-Difference Time-Domain (FDTD) Method for Electromagnetics*, Morgan & Claypool, 2011.

50. Born, M. and E. Wolf, *Principles of Optics: Electromagnetic Theory of Propagation, Interference and Diffraction of Light*, 7th Edition, Cambridge University Press, Oct. 1999.

51. Bhalla, R. and H. Ling, "Three-dimensional scattering center extraction using the shooting and bouncing ray technique," *IEEE Antennas and Propag. Mag.*, Vol. 44, No. 11, 1445–1453, Nov. 1996.

52. Ufimtsev, P., *Theory of Edge Diffraction in Electromagnetics: Origination and Validation of the Physical Theory of diffraction*, Revised Edition, Scitech Publishing, Jun. 2009.

53. FEKO-EM Simulation, [Online], Available: https://www.feko.info/.

54. Maxwell's equations, [Online], Available: https://en.wikipedia.org/wiki/Maxwell%27s_equations.

55. Matrix representation of Maxwell's equations, [Online], Available: https://en.wikipedia.org/wiki/Matrix_representation_of_Maxwell%27s_equations.

56. Basic Principle of the Method of Moments, [Online], Available: http://www.emagtech.com/wiki/index.php/Basic_Principles_of_The_Method_of_Moments.

57. Chew, W. C., J.-M. Jin, E. Michielssen, and J. Song, *Algorithms in Computational Electromagnetic*, Artech House, 2001.

58. Alves, M. A., I. M. Martins, M. A. S. Miacci, and M. C. Rezende, "Radar cross section of simple and complex targets in the C-band: A comparison between anechoic chamber measurements and simulations," *PIERS Online*, Vol. 4, No. 7, 791–794, 2008.

59. Boeing T-X Trainer Aircraft, [Online], Available: https://www.airforce-technology.com/projects/boeing-t-x-trainer-aircraft/.